

Numerical simulation of light backscattering by spheres with off-center inclusion. Application to the lidar case

Vadim Griaznov, Igor Veselovskii, Paolo Di Girolamo, Belay Demoz, and David N. Whiteman

A Mie backscattering model for spherical particles with off-center inclusion has been developed and tested. The program is capable of dealing with size parameter values up to ~ 1000 , thus allowing one to simulate the optical behavior of a large variety of atmospheric aerosols, as well as cloud and precipitation particles. On the basis of this model, we simulated the optical properties of polydisperse composite atmospheric particles as observed by ground-based and airborne lidar systems. We have characterized optical properties in terms of host and inclusion radii, considering water particles with different composition inclusions. The performed modeling provides some insight into the so-called lidar bright- and dark-band phenomenon. © 2004 Optical Society of America

OCIS codes: 010.1310, 010.3640, 280.1310, 290.4020.

1. Introduction

Determination of the microphysical properties of atmospheric aerosols from optical remote-sensed data is often done with the use of complex scattering models. The Mie theory provides rigorous solutions for light scattering by isotropic spheres embedded in a homogeneous medium.¹ Extensions of Mie theory include solutions for core-shell spheres and gradient-index spheres. Although these theories are restricted to the case of perfect spheres, the results have provided insight into the scattering and absorption properties for a wide variety of atmospheric particles, including nonspherical particles. The mathematics of Mie theory is straightforward but tedious, requiring the computation of a potentially large number of series expansions, which makes the computations for big particles extremely time consuming. Alternatively, the application of Monte Carlo ray-tracing models based on geometrical-optics

methods allows one to consider particles with irregular shape and with a variety of inclusions. However, this approach may fail for large sizes because of its inability to treat circumferentially backscattered surface waves² and its inability to properly reproduce resonance phenomena. Additionally, the concepts of geometrical optics do not adequately describe the interactions of particles with light when the particle size is comparable with the wavelength of the light. The transformation of aerosols into cloud particles and hydrometeors involves a number of different physical processes, which permit particles to grow from the sizes of cloud condensation nuclei (typically $0.1 \mu\text{m}$) to sizes in excess of $1000 \mu\text{m}$. UV- and visible-wavelength-based study of the microphysical processes involved in the formation of clouds and precipitations requires scattering codes that allow one to deal with size parameter values in excess of 5000^3 and are capable of considering the combined particles consisting of host and inclusion.

One of the topics actively studied at present with the use of radars and lidars is the change in scattering properties of melting hydrometeors. Such changes take place during the snowflake-to-raindrop transition in the proximity of the freezing level, leading to a minimum in particle backscatter at optical wavelengths⁴ (Sassen and Chen). Although not quite exact, melting hydrometeors are frequently modeled as a two-layered particle, consisting of a water shell about an inner core of snow or ice.⁵⁻⁹ An

V. Griaznov and I. Veselovskii (iveselov@agnes.gsfc.nasa.gov) are with the Physics Instrumentation Center of the General Physics Institute, Troitsk, Moscow Region, 142190, Russia. P. Di Girolamo is with the Università degli Studi della Basilicata, Potenza, Italy. B. Demoz and D. N. Whiteman are with the NASA Goddard Space Flight Center, Greenbelt, Maryland 20771-0001.

Received 12 January 2004; revised manuscript received 18 June 2004; accepted 13 July 2004.

0003-6935/04/295512-11\$15.00/0

© 2004 Optical Society of America

approximation for such a two-layered particle may be represented by the eccentric spheres model¹⁰: The core can float to the top of the water drop because of entrapped air bubbles. The first attempt to simulate the melting of ice particles with the use of Mie code for eccentric spheres and apply it to the dark- and bright-band phenomenon was made by Di Girolamo *et al.*³ The authors used the scattering code developed by Mackowski,¹¹ which could perform calculations for monodisperse particles with size parameters as large as $x \sim 100$. The obtained results demonstrate the importance of eccentric model implementation, but the huge computation time did not allow consideration of the polydisperse aerosol of sufficient size to make final conclusions about the changes of scattering properties that may occur in real atmosphere.

In the present paper we first describe the development of an eccentric model capable of handling size parameter values as large as 1000. On the basis of rigorous Mie theory, the model allows simulation of the backscattering properties of two-phase aerosol particles in the form of eccentric spheres. We have applied the model here to study the changes in scattering properties of melting ice spheres, getting some insight into the so-called lidar bright- and dark-band phenomenon. This subject will be discussed in Section 4.

The structure of the paper is as follows: Section 2 describes the mathematics implemented in the model, Section 3 describes the simulations performed, and Section 4 is dedicated to the discussion of the results.

2. General Expressions

Light scattering by spheres with nonconcentric spherical inclusions has been considered in publications.^{10–15} All these algorithms are based on a recurrence approach to calculate the scalar and vector coefficients for translation of vector spherical harmonics from one coordinate system, adjusted to the center of the inclusion, to another, adjusted to the host particle center. Though the expressions derived in Refs. 11 and 15 allow one to make the calculation at any scattering angle for an arbitrary position of the inclusion inside the host sphere, the computation time increases fast with increase in the particle radius. Existing computer codes can be used only for spheres with size parameters $x \sim 100$ (size parameter for a host sphere with radius a_1 is $x = 2\pi a_1/\lambda$), whereas realistic modeling of clouds by lidar requires consideration of particles with $x \sim 1000$.

To simplify the formulas and thus decrease the computation time, we make the following caveats in the algorithm presented here.

- We consider only light backscattering—the relevant measure in lidar measurements.
- We limit the movement of the inclusion to be along the axis of the direction of incident light propagation. Such simplification should be reasonable; for example, in the case of an ice nucleus floating in a

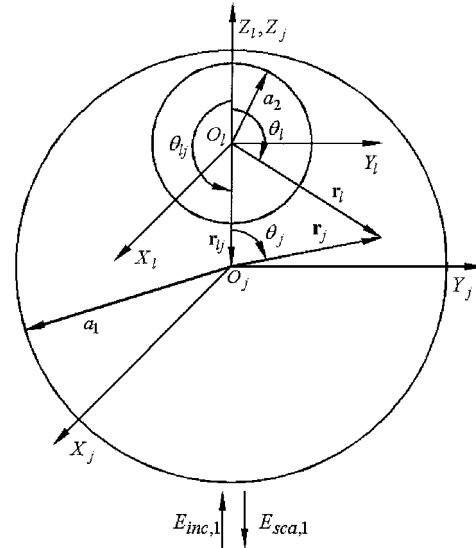


Fig. 1. Geometry of scattering.

water droplet, we assume only vertical lidar measurements.

The geometry of scattering, together with the description of the main symbols, is presented in Fig. 1. Because we are considering backscattered light only, the expressions presented in Refs. 11 and 15 will be simplified essentially. First, the incident wave may be expanded as¹⁵

$$\mathbf{E}_{inc,1} = \sum_{n=1}^{\infty} \sum_{m=-n}^n [a_{nm} \mathbf{M}_{nm}^{(1)} + b_{nm} \mathbf{N}_{nm}^{(1)}], \quad (1)$$

where $\mathbf{M}_{n,m}^{(j)}(\mathbf{r})$ and $\mathbf{N}_{n,m}^{(j)}(\mathbf{r})$ are vector spherical harmonics described in detail in Ref. 15 and the subscript 1 corresponds to the upward direction of incident light. The incident wave propagates along the OZ axis; therefore it does not contain terms with index $m \neq \pm 1$. As a result, the scattered field

$$\mathbf{E}_{sca,1} = \sum_{n=0}^{\infty} \sum_{m=-n}^n [c_{nm} \mathbf{M}_{nm}^{(3)} + d_{nm} \mathbf{N}_{nm}^{(3)}] \quad (2)$$

does not contain these terms. Second, the values of multipole coefficients c_{nm} , d_{nm} for indices $m = -1$ may be expressed through the corresponding coefficients at $m = 1$ as pointed out below. Therefore it is sufficient to solve the system of equations¹⁵ only once, for $m = 1$. In the subsequent text all the formulas are derived from the corresponding equations given in Ref. 11, except that the spherical Bessel functions are replaced by Riccati–Bessel functions and Legendre functions $P_n^m(\cos \theta)$ are not normalized and contain multiplier $(-1)^m$ according to Ref. 16.

The first step in the calculations is finding all scalar translation coefficients $C_{0,n}^{0,0}$ for indices from $n = 0$ to $n = n_{max}$ by use of the relation

$$k_1 r_{ij} C_{0,n}^{0,0} = (2n + 1) \psi_n(k_1 r_{ij}), \quad r_j \geq r_{ij}, \quad (3)$$

for downward translation (angle $\theta_{lj} = 180^\circ$). Here k_1 is the wave number in the host particle, r_{lj} is the distance between the host and the inclusion centers, and $\psi_n(k_1 r_{lj})$ denotes Riccati–Bessel functions of the first kind.

If the inclusion is placed below the center of the host particle, the translation is performed upward from the system l to j and $\theta_{lj} = 0^\circ$. In this case we should use the relation

$$k_1 r_{lj} C_{0,n}^{0,0} = (-1)^n (2n + 1) \psi_n(k_1 r_{lj}), \quad r_j \geq r_{lj}. \quad (4)$$

At the next step the scalar coefficients for index $\nu = 1$ can be determined from formulas

$$k_1 r_{lj} C_{0,n}^{0,1} = n \psi_{n-1}(k_1 r_{lj}) - (n + 1) \psi_{n+1}(k_1 r_{lj}), \quad (5)$$

$$k_1 r_{lj} C_{0,n}^{0,1} = (-1)^{n-1} [n \psi_{n-1}(k_1 r_{lj}) - (n + 1) \psi_{n+1}(k_1 r_{lj})], \quad (6)$$

respectively, for downward and upward translations.

From the first additional formula for scalar coefficients¹¹ taken for $\xi = \eta = 0$, we have

$$C_{m+1,n}^{m+1,\nu} = \frac{k_1 Z_{lj} C_{m,n+1}^{m,\nu}}{2n + 3} + \frac{k_1 Z_{lj} C_{m,n-1}^{m,\nu}}{2n - 1} + C_{m,n}^{m,\nu}.$$

After further substituting $m = 0$, $\nu = 1$, $\theta_{lj} = 180^\circ$, and $Z_{lj} = r_{lj} \cos \theta_{lj} = -r_{lj}$ into the above relation, it becomes

$$C_{1,n}^{1,1} = C_{0,n}^{0,1} - k_1 r_{lj} \left(\frac{C_{0,n+1}^{0,1}}{2n + 3} + \frac{C_{0,n-1}^{0,1}}{2n - 1} \right). \quad (7)$$

For the upward translation we have, correspondingly,

$$C_{1,n}^{1,1} = C_{0,n}^{0,1} + k_1 r_{lj} \left(\frac{C_{0,n+1}^{0,1}}{2n + 3} + \frac{C_{0,n-1}^{0,1}}{2n - 1} \right). \quad (8)$$

Using formulas for $C_{0,n}^{0,1}$, $C_{0,n+1}^{0,1}$, and $C_{0,n-1}^{0,1}$ and recurrence relations for spherical Bessel functions, we obtain, for the scalar coefficients with index $m = 1$ and angle $\theta_{lj} = 180^\circ$,

$$C_{1,n}^{1,1} = \frac{(2n + 1) \psi_n(k_1 r_{lj})}{(k r_{lj})^2}. \quad (9)$$

For $\theta_{lj} = 0^\circ$, this formula becomes

$$C_{1,n}^{1,1} = (-1)^{n-1} \frac{(2n + 1) \psi_n(k_1 r_{lj})}{(k r_{lj})^2}. \quad (10)$$

From the third recurrence formula for scalar coefficients¹¹ taken at index $\nu = 2$, we find for the downward translation ($\theta_{lj} = 180^\circ$)

$$C_{1,n}^{1,2} = 3 \left(\frac{n - 1}{2n - 1} C_{1,n-1}^{1,1} - \frac{n + 2}{2n + 3} C_{1,n+1}^{1,1} \right). \quad (11)$$

For the upward translation ($\theta_{lj} = 0^\circ$) we can use a more simple relationship:

$$C_{1,n}^{1,2}(0^\circ) = (-1)^n C_{1,n}^{1,2}(180^\circ). \quad (12)$$

The coefficients for indices $\nu = 2, 3, \dots, \nu_{\max}$ and $\theta_{lj} = 180^\circ$ can be found from the formula

$$C_{1,n}^{1,\nu} = \frac{2\nu - 1}{\nu - 1} \left(\frac{\nu}{2\nu - 1} C_{1,n}^{1,\nu-2} - \frac{n + 2}{2n + 3} C_{1,n+1}^{1,\nu-1} + \frac{n - 1}{2n - 1} C_{1,n-1}^{1,\nu-1} \right), \quad (13)$$

which is derived from the same equation¹¹ that was used above. For the upward translation it is convenient to use the simple relationship

$$C_{1,n}^{1,\nu}(0^\circ) = (-1)^{n+\nu} C_{1,n}^{1,\nu}(180^\circ). \quad (14)$$

From additional Mackowski's formulas¹¹ for vector translation coefficients $A_{m,n}^{\mu,\nu}$ and $B_{m,n}^{\mu,\nu}$ taken at $m = \mu = 1$, $\xi = \eta = 0$, $n = 1, 2, \dots, n_{\max}$, $\nu = 1, 2, \dots, \nu_{\max}$, and $\theta_{lj} = 180^\circ$, we have

$$A_{1,n}^{1,\nu} = C_{1,n}^{1,\nu} - k_1 r_{lj} \left[\frac{(n + 2)}{(n + 1)(2n + 3)} C_{1,n}^{1,\nu} + \frac{(n - 1)}{n(2n - 1)} C_{1,n-1}^{1,\nu} \right], \quad (15)$$

$$B_{1,n}^{1,\nu} = -i k_1 r_{lj} \frac{C_{1,n}^{1,\nu}}{n(n + 1)} \quad (16)$$

and, correspondingly, for $\theta_{lj} = 0^\circ$:

$$A_{1,n}^{1,\nu} = C_{1,n}^{1,\nu} + k_1 r_{lj} \left[\frac{(n + 2)}{(n + 1)(2n + 3)} C_{1,n+1}^{1,\nu} + \frac{(n - 1)}{n(2n - 1)} C_{1,n-1}^{1,\nu} \right], \quad (17)$$

$$B_{1,n}^{1,\nu} = +i k_1 r_{lj} \frac{C_{1,n}^{1,\nu}}{n(n + 1)}. \quad (18)$$

The relations between coefficients at two opposite shifts of the coordinate system l relative to the system j are as follows:

$$A_{1,n}^{1,\nu}(0^\circ) = (-1)^{n+\nu} A_{1,n}^{1,\nu}(180^\circ), \quad (19)$$

$$B_{1,n}^{1,\nu}(0^\circ) = -(-1)^{n+\nu} B_{1,n}^{1,\nu}(180^\circ). \quad (20)$$

For the calculation of multipole coefficients c_{nm} , d_{nm} of the scattered field, we first determine the unknowns t_{vm} , u_{vm} from the system of equations¹⁵

$$\left\{ \begin{array}{l} \sum_{v=1}^{v_{\max}} t_{vm} T_{1,m,v}^A + u_{vm} U_{1,m,v}^B = a_{1m} n_1 i \\ \sum_{v=1}^{v_{\max}} t_{vm} T_{2,m,v}^A + u_{vm} U_{2,m,v}^B = a_{2m} n_1 i \\ \dots\dots\dots \\ \sum_{v=1}^{v_{\max}} t_{vm} T_{n_{\max},m,v}^A + u_{vm} U_{n_{\max},m,v}^A = a_{n_{\max}m} n_1 i \\ \sum_{v=1}^{v_{\max}} t_{vm} T_{1,m,v}^B + u_{vm} U_{1,m,v}^A = b_{1m} n_1 i \\ \sum_{v=1}^{v_{\max}} t_{vm} T_{2,m,v}^B + u_{vm} U_{2,m,v}^A = b_{2m} n_1 i \\ \dots\dots\dots \\ \sum_{v=1}^{v_{\max}} t_{vm} T_{n_{\max},m,v}^A + u_{vm} U_{n_{\max},m,v}^A = b_{n_{\max}m} n_1 i \end{array} \right. , \quad (21)$$

where

$$T_{n,m,v}^A = A_{m,n}^{m,v} \{ \xi'_n(ka_1) [\zeta_n(k_1 a_1) + Q_v^r \xi_n(k_1 a_1)] - n_1 \xi_n(ka_1) [\zeta'_n(k_1 a_1) + Q_v^r \xi'_n(k_1 a_1)] \}, \quad (22)$$

$$U_{n,m,v}^B = B_{m,n}^{m,v} \{ \xi'_n(ka_1) [\zeta_n(k_1 a_1) + Q_v^s \xi_n(k_1 a_1)] - n_1 \xi_n(ka_1) [\zeta'_n(k_1 a_1) + Q_v^s \xi'_n(k_1 a_1)] \}, \quad (23)$$

$$T_{n,m,v}^B = B_{m,n}^{m,v} \{ n_1 \xi'_n(ka_1) [\zeta_n(k_1 a_1) + Q_v^r \xi_n(k_1 a_1)] - \xi_n(ka_1) [\zeta'_n(k_1 a_1) + Q_v^r \xi'_n(k_1 a_1)] \}, \quad (24)$$

$$U_{n,m,v}^A = A_{m,n}^{m,v} \{ n_1 \xi'_n(ka_1) [\zeta_n(k_1 a_1) + Q_v^s \xi_n(k_1 a_1)] - \xi_n(ka_1) [\zeta'_n(k_1 a_1) + Q_v^s \xi'_n(k_1 a_1)] \}, \quad (25)$$

$$Q_v^r = \frac{n_1 \zeta'_v(k_1 a_2) \psi_v(k_2 a_2) - n_2 \zeta_v(k_1 a_2) \psi'_v(k_2 a_2)}{n_2 \xi_v(k_1 a_2) \psi'_v(k_2 a_2) - n_1 \xi'_v(k_1 a_2) \psi_v(k_2 a_2)}, \quad (26)$$

$$Q_v^s = \frac{n_2 \zeta'_v(k_1 a_2) \psi_v(k_2 a_2) - n_1 \zeta_v(k_1 a_2) \psi'_v(k_2 a_2)}{n_1 \xi_v(k_1 a_2) \psi'_v(k_2 a_2) - n_2 \xi'_v(k_1 a_2) \psi_v(k_2 a_2)}. \quad (27)$$

Here a_1 and a_2 are radii of the host and inclusion particles, respectively; n_1 and n_2 are their refractive indices; k and k_2 denote wave numbers of the outer medium and inclusion; ξ_n and ζ_n are Riccati–Bessel functions of the third and fourth kinds; and primes denote derivatives. After the unknowns t_{vm} , u_{vm} are

found, the multipole coefficients c_{nm} , d_{nm} of the scattered field \mathbf{E}_{sca} can be found with formulas

$$c_{nm} = \frac{1}{n_1 \xi_n^2(ka_1)} \times \sum_{v=1}^{v_{\max}} \left\{ \frac{t_{vm} T_{n,m,v}^A}{\xi'_n(ka_1) - n_1 \left[\frac{\zeta'_n(k_1 a_1) + Q_v^r \xi'_n(k_1 a_1)}{[\zeta_n(k_1 a_1) + Q_v^r \xi_n(k_1 a_1)]} \right]} + \frac{u_{vm} U_{n,m,v}^B}{\xi_n(ka_1) - n_1 \left[\frac{\zeta'_n(k_1 a_1) + Q_v^s \xi'_n(k_1 a_1)}{[\zeta_n(k_1 a_1) + Q_v^s \xi_n(k_1 a_1)]} \right]} \right\} - a_{nm} \frac{\psi_n(ka_1)}{\xi_n(ka_1)}, \quad (28)$$

$$d_{nm} = \frac{1}{\xi_n^2(ka_1)} \times \sum_{v=1}^{v_{\max}} \left\{ \frac{t_{vm} T_{n,m,v}^B}{n_1 \left[\frac{\xi'_n(ka_1)}{\xi_n(ka_1)} - \frac{[\zeta'_n(k_1 a_1) + Q_v^r \xi'_n(k_1 a_1)]}{[\zeta_n(k_1 a_1) + Q_v^r \xi_n(k_1 a_1)]} \right]} + \frac{u_{vm} U_{n,m,v}^A}{n_1 \left[\frac{\xi'_n(ka_1)}{\xi_n(ka_1)} - \frac{[\zeta'_n(k_1 a_1) + Q_v^s \xi'_n(k_1 a_1)]}{[\zeta_n(k_1 a_1) + Q_v^s \xi_n(k_1 a_1)]} \right]} \right\} - b_{nm} \frac{\psi_n(ka_1)}{\xi_n(ka_1)}, \quad (29)$$

taken at $m = 1$.

For calculations of these coefficients at $m = -1$, we use simple relations:

$$c_{n,-1} = n(n+1)c_{n,1}, \quad (30)$$

$$d_{n,-1} = -n(n+1)d_{n,1}. \quad (31)$$

Finally, the backscattering cross section $d\sigma/d\Omega$ and extinction cross section σ_{ext} ^{11,15} are given by

$$\frac{d\sigma}{d\Omega} = \frac{\lambda^2}{4\pi^2} \left| \sum_{n=1}^{\infty} i^n n(n+1)(c_{n,1} - d_{n,1}) \right|^2, \quad (32)$$

$$\sigma_{\text{ext}} = -\frac{2\pi}{k^2} \text{Re} \left\{ \sum_{n=1}^{\infty} n(n+1) i^{n+1} [c_{n,1}^* + (-1)^{n+1} c_{n,1} + (-1)^{n+1} d_{n,1} + d_{n,1}^*] \right\}. \quad (33)$$

The last two formulas also give us the opportunity to compare results obtained by upward-looking lidar (incident wave $\mathbf{E}_{\text{inc},1}$, see Fig. 1) with data received by downward-looking lidar radiating incident wave $\mathbf{E}_{\text{inc},2}$ in the opposite direction. The backscattering coefficients for these two situations will be different, whereas the extinction coefficients will be the same, i.e., $\sigma_{\text{ext},2} = \sigma_{\text{ext},1}$. This fact is proved in Appendix A.

3. Simulation Results

We have computer coded the above equations, and we discuss the simulation results below. Our main focus is to attempt to understand the scattering properties of combined hydrometeors, consisting of a spherical host and a spherical inclusion, and how these may be revealed in lidar experiments. For describing the optical signal detected by lidar, the optical parameters that are commonly considered are backscattering β and extinction α coefficients and their ratio, $R = \alpha/\beta$, known as a lidar ratio. These quantities are the main scattering parameters that we will evaluate by the simulation. The main questions that we address in our study are how the particle scattering properties depend on the inclusion size, on its location inside the host, and on their refractive indices. We will further simplify the question by assuming that the refractive index of the host in our calculations is set to $m_h = 1.348 - i0$, which corresponds to pure water at 355 nm, whereas the refractive index of the inclusion may be higher or lower than that of the host. We will use $m_i = 1.45 - i0$ and $m_i = 1.25 - i0$ to represent the situations when $m_i > m_h$ (dust particles) and $m_i < m_h$ (biological particles), respectively. The case of special interest here is a water droplet with an ice inclusion; the corresponding value of the refraction index is $m_i = 1.324 - i0$.¹⁷

Our computer program allows for computations for spheres with size parameters of as large as ~ 1000 . In the simulation, computation time increases with size parameter approximately as x^4 , and computation time (for a typical scenario considered below) at $x = 1000$ took more than a week on a 2.3-GHz personal computer. Understandably, we usually limited our computations to $x < 500$. Simulation results for small size parameters were compared with those from Mackowski,¹¹ and, for an inclusion located in the center of the host, results were compared with a concentric spheres code.³ In both cases the results proved to be in agreement with existing programs.

A. Dependence of Scattering Properties on Inclusion Size

To evaluate the dependence of particle scattering parameters on an inclusion relative radius (ρ defined here is the ratio of the radius of the inclusion to the radius of the host particle a_2/a_1), we first consider the condition in which the inclusion is attached to the top or bottom of the host, i.e., $\rho + \delta \approx \pm 1$. Here $\delta = (r_{ij}/a_1)\cos\theta_{ij} = \pm r_{ij}/a_1$ is an inclusion relative shift (r_{ij} is the distance between the host and the inclusion centers), $\delta = 1$ corresponds to an infinitely small inclusion attached to the top of the host sphere, and $\delta = -1$ when the inclusion is at the bottom. So changing ρ from 0 to 1 corresponds to the following: The small inclusion starts near the top of the host particle and increases in size, until it fills the entire host sphere. To some extent, such geometry corresponds, for example, to the case of an ice sphere melting while the unmelted floating core stays near the top of the water particle.

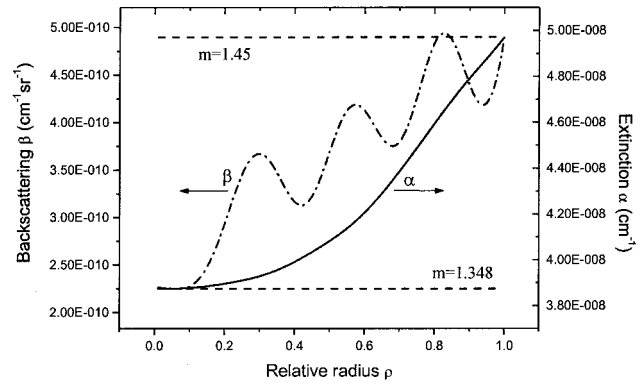


Fig. 2. Extinction and backscattering coefficients as a function of the inclusion relative radius. The inclusion with $m_i = 1.45$ is fixed near the top of the host sphere with $m = 1.348$ and size parameter $x = 4$. Dashed lines show the extinction and backscattering for the host sphere without an inclusion.

This configuration is illustrated by Fig. 2, in which the calculations are performed for $x = 4$, $m_i = 1.45$, and $\rho + \delta = 0.995$. Dashed lines show α and β values for homogenous spheres with refractive indices 1.348 and 1.45. Solid and dashed-dotted curves are simulated values for inclusion nuclei that start at the top and gradually fill the host particle. At a small inclusion radius the particle extinction is determined by the refractive index of the host sphere. With ρ increasing, the extinction is enhanced, and, finally, when the inclusion fills the whole sphere, extinction is practically that of the inclusion itself. The backscattering coefficient is changed in a similar manner, though it is more oscillatory.

For large particles the picture becomes more complicated as shown in Fig. 3. This figure shows the dependence of the same parameters for $x = 200$ (the size parameter x of the host sphere is chosen not to coincide with one of the morphology-dependent resonances). Both β and α are normalized to the corresponding values of the host particle without an inclusion. Such normalization allows one to compare the effect of an inclusion on scattering properties of host particles with different size parameters. Curves are shown for the inclusion fixed to the top (solid curve) or bottom (dotted curve) of the host sphere, and the dashed-dotted curve represents the results obtained for a concentric spheres model. Calculations are performed with a step of $\Delta\rho = 0.01$. A notable result is the fact that $\alpha(\rho)$ is not dependent on where the inclusion is fixed (top or bottom) in the host particle; the curves coincide perfectly. We have also shown that this is true in the derivation we present in Appendix A. For big spheres without absorption, the extinction deviates slightly from 1 and is not too sensitive to changes in ρ . The dependence of β on ρ , however, is complicated because of numerous resonance effects.

To further investigate the dependence of β on ρ and to determine the scattering features slowly changing with particle size, we performed a simulation for

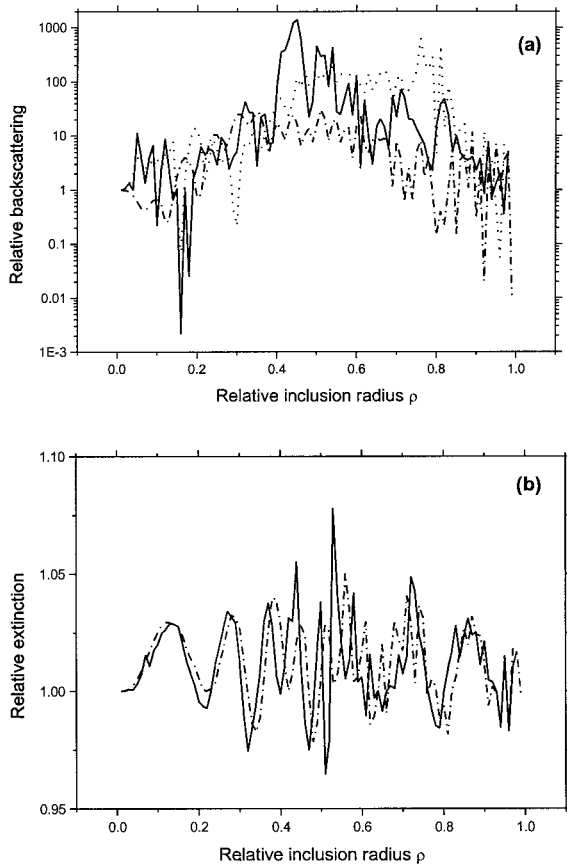


Fig. 3. Relative (a) backscattering and (b) extinction coefficients as a function of relative inclusion radius. Calculations are performed for a host sphere with $x = 200$, $m_h = 1.348$, and $m_i = 1.45$. The inclusion is fixed to the top (solid curve) or bottom (dotted curve) of the host sphere. The dashed-dotted curve presents the results obtained for concentric spheres. The calculation step is $\Delta\rho = 0.01$.

polydisperse spheres. We assumed a log-normal distribution for a_1 but kept the ratio ρ the same for all particles. The size distribution was used in the form

$$n_N(a_1) = \frac{1}{\sqrt{2\pi} a_1 \ln \sigma} \exp\left[-\frac{(\ln a_1 - \ln a_{1,\text{mean}})^2}{2 \ln^2 \sigma}\right],$$

where $\ln a_{1,\text{mean}}$ is the mean radius of the host sphere and $\ln^2 \sigma$ is the dispersion. We should point out here that the choice of the size distribution was not aimed to match any real atmospheric situation but rather to investigate if we can remove the effects related to morphology-dependent resonances. The number of points inside this distribution was usually taken as $N = 30$, to keep computation time manageable.

Figure 4 shows the results obtained for a distribution with $x_{\text{mean}} = 300$ and $\ln \sigma = 0.1$ (x varies between 200 and 400). Refractive indices of the host particle and its inclusion are $m_h = 1.348$ and $m_i = 1.45$. The calculation step used is $\Delta\rho = 0.02$, and the results are smoothed over a 0.06 interval. Results for the same configurations as in Fig. 3 are shown: The inclusion is fixed to the top or bottom of the host

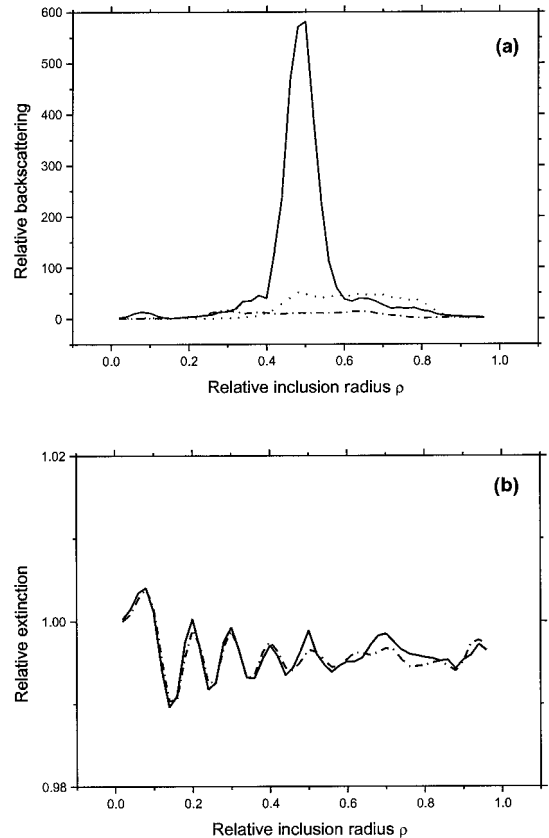


Fig. 4. Dependence of relative (a) backscattering and (b) extinction coefficients on the inclusion relative radius. The inclusion is fixed to the top (solid curve) or to the bottom (dotted curve) of the host particle, and the dashed-dotted curve shows the result for concentric spheres. Calculations are performed for log-normal distribution of host spheres' radii with $x_{\text{mean}} = 300$ and $\ln \sigma = 0.1$. Refractive indices of the host particle and inclusion are $m_h = 1.348$ and $m_i = 1.45$, respectively. The calculation step is $\Delta\rho = 0.02$, and the obtained results are smoothed with a 0.06 averaging interval.

sphere and for concentric spheres. When the inclusion was located near the top of the host sphere center, an increase in backscattering of almost 3 orders of magnitude is observed for $\rho \sim 0.5$. For the inclusion located near the sphere bottom, $\rho \sim 0.5$ resulted only in 1 order of magnitude in backscatter enhancement, and the enhancement for concentric spheres is not significant. Another interesting result is the fact that the change in extinction of the combined particle did not exceed 1% for all ρ values.

B. Dependence of Scattering Properties on Refractive Index

To study the effect of the refractive index, we performed calculations for the same geometrical considerations but for inclusions with refractive index $m_i = 1.25$ (Fig. 5). Dramatically different results are obtained in that the maximum enhancement in backscattering occurs when the inclusion is located near the bottom of the host sphere and $\rho \approx 0.85$. For the case of an inclusion set at the top of the host particle,

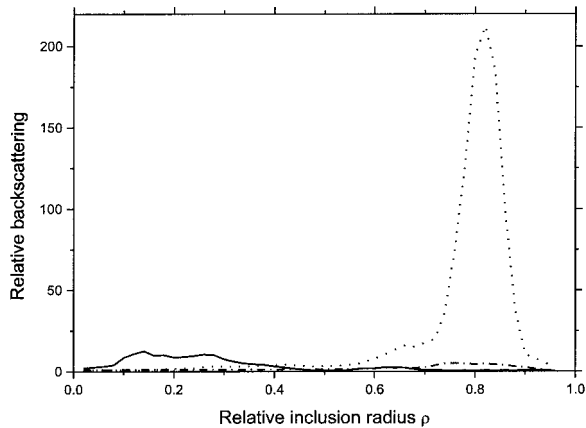


Fig. 5. Dependence of relative backscattering on the inclusion relative radius. The inclusion is fixed to the top (solid curve) or to the bottom (dotted curve) of the host particle, and the dashed-dotted curve shows the result for concentric spheres. Calculations are performed for log-normal distribution of host spheres' radii with $x_{\text{mean}} = 300$ and $\ln \sigma = 0.1$. Refractive indices of the host particle and inclusion are $m_h = 1.348$ and $m_i = 1.25$, respectively. The calculation step is $\Delta\rho = 0.02$, and the obtained results are smoothed with a 0.06 averaging interval.

measurable backscatter enhancement is observed for $\rho < 0.5$ and with no or even a decrease in backscatter for larger inclusions. The normalized extinction is close to 1, hence the relative lidar ratio $R \approx 1/\beta$; i.e., the relative lidar ratio differs strongly for an inclusion located near the top or bottom of the host sphere. This suggests that the lidar ratio for such particles (to the extent they are applicable) will be different for measurements performed from the ground and from an aircraft.

Figures 4 and 5 dealt with only two values of m_i , whereas in Fig. 6 we show a simulation for varying m_i for top ($m_i > m_h$) and bottom ($m_i < m_h$) inclusion locations, where maximum backscattering enhancement is observed. The results may be summarized as follows. For $m_i > m_h$, the maximum backscattering enhancement is observed at $\rho \approx 0.5$ for all m_i tested. It is interesting to note that the maximal backscattering enhancement (relative $\beta \approx 450$) corresponds to $m_i = 1.4$ and slightly decreases with increase in m_i . But, for the case of $m_i < m_h$, backscattering is enhanced at $\rho \approx 0.8$ for all m_i in the range 1.15–1.3 and increases with decreasing m_i , reaching a maximum value of $\beta \approx 1200$ at $m_i = 1.15$.

The dependence of maximal backscattering on the inclusion refractive index is nicely summarized in Fig. 7. Note that the highest backscattering enhancement is obtained for $m_i = 1$, which corresponds to an air bubble inside the water sphere. For $m_i > 1.4$, the maximum value of backscattering enhancement does not change significantly.

A comparison of these results with those from concentric sphere geometry for scenarios similar to those in Fig. 6 yields interesting conclusions (Fig. 8). For $m_i > m_h$, the maximums in backscattering

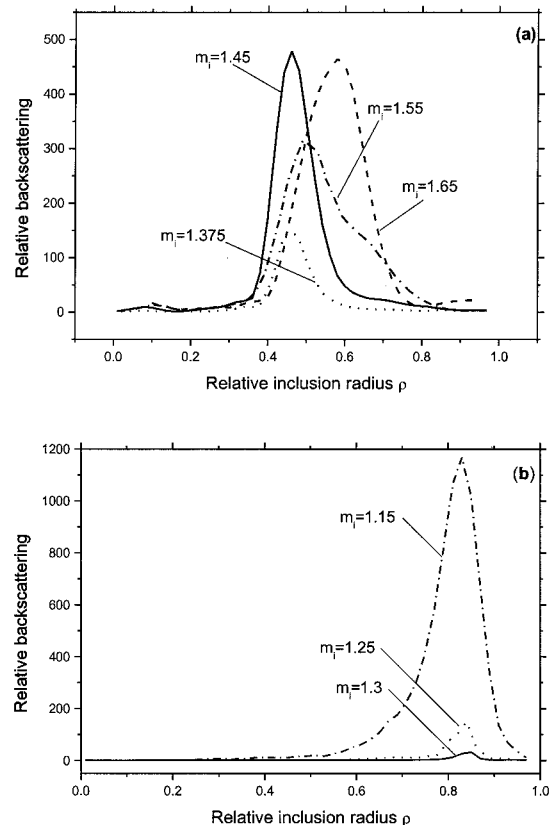


Fig. 6. Dependence of relative backscattering on the inclusion relative radius for (a) $m_i > m_h$ and (b) $m_i < m_h$. The inclusion is fixed to the (a) top or (b) bottom of the host particle. Host spheres' radii are log-normal distributed with $x_{\text{mean}} = 200$ and $\ln \sigma = 0.1$. The calculation step is $\Delta\rho = 0.02$, and the obtained results are smoothed with a 0.06 averaging interval.

are centered at $\rho \approx 0.5$ and, for $m_i < m_h$, the center is shifted to $\rho \approx 0.8$. These results are in agreement with those discussed in Ref. 3 for melting ice spheres. In contrast to the nonconcentric model, the relative β enhancement for concentric spheres is lower, though the peaks are wider. The differ-

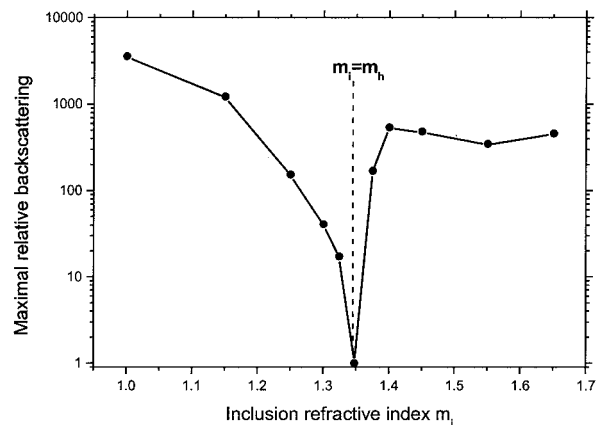


Fig. 7. Dependence of maximal relative backscattering on the inclusion refractive index. Host spheres' radii are log-normal distributed with $x_{\text{mean}} = 200$ and $\ln \sigma = 0.1$.

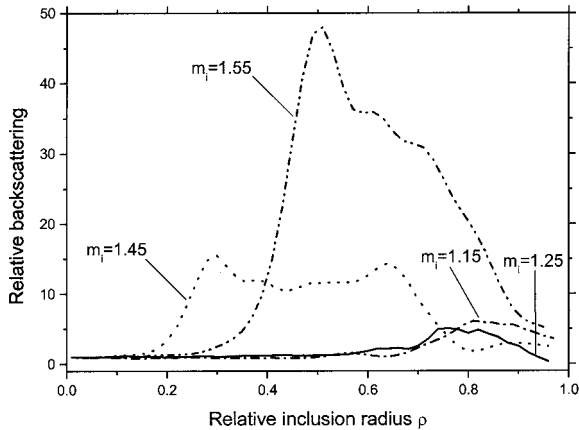


Fig. 8. Relative backscattering as a function of the relative inclusion radius calculated for concentric spheres with $m_i = 1.15$ (dashed-dotted curve), 1.25 (solid curve), 1.45 (dotted curve), and 1.55 (dashed-dotted-dotted curve). The calculation step is $\Delta\rho = 0.02$, and the obtained results are smoothed with a 0.06 averaging interval.

ence is especially significant for $m_i < m_h$. For concentric spheres at $m_i = 1.15$, the maximum enhancement is $\beta \approx 5$, which is more than 2 orders lower than enhancement in the nonconcentric model.

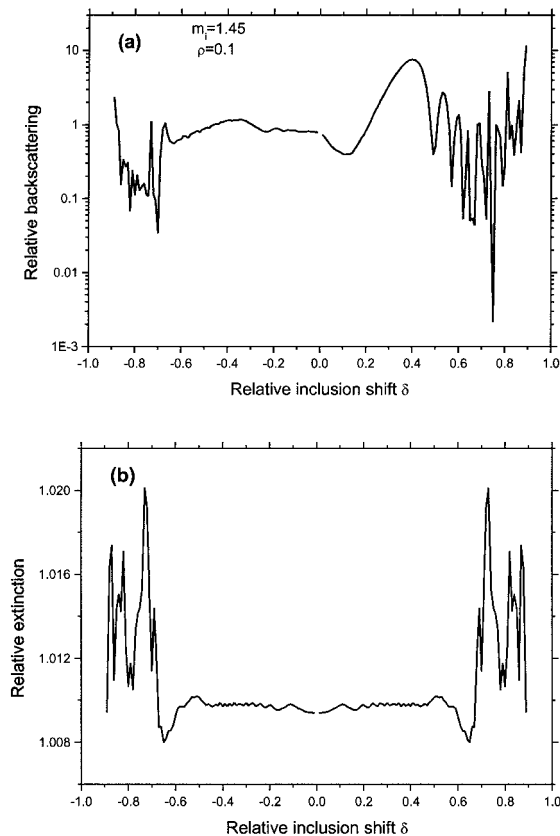


Fig. 9. Dependence of relative (a) backscattering and (b) extinction on the relative inclusion shift. Calculations are performed for monodisperse spheres with $x = 200$, $\rho = 0.1$, $m_h = 1.348$, and $m_i = 1.45$. The calculation step is $\Delta\delta = 0.01$.

C. Dependence of Scattering Properties on Vertical Displacement of the Inclusion

In this subsection we present the results of numerical simulations performed to understand how a vertical shift in the position of the inclusion of constant size influences the particle scattering properties. The dependence of backscattering and extinction coefficients on the relative inclusion shift for $\rho = 0.1$ and $m_i = 1.45$ is presented in Fig. 9. The calculations in the figure are performed for a single sphere with $x = 200$ and a calculation step of $\Delta\delta = 0.01$. The dependence α on the relative shift is symmetric relative to the center of the host sphere. This is in agreement with previous statements and the results shown in Appendix A.

The behavior of backscattering is, however, complicated by morphology-dependent resonance effects. Here again we consider a distribution of sizes to see how it affects these resonances (Fig. 10). The calculations are made for inclusions with relative radii of $\rho = 0.1, 0.5$, and 0.8 and a log-normal distribution of host spheres with mean radii of $x_{\text{mean}} = 300$ and $\ln \sigma = 0.1$. Refractive indices of the host particle and inclusion are $m_h = 1.348$ and $m_i = 1.45$, respectively, and a calculation step of $\Delta\delta = 0.02$ is used. The results plotted in Fig. 10 are smoothed over a 0.06 averaging interval. Similar to our earlier results (see discussion of Fig. 4), backscattering is most sensitive to the translation when the inclusion relative radius is of $\rho = 0.5$ and reaches a maximum when the inclusion is located near the top of the sphere. When the inclusion is located near the bottom of the host sphere, the relative backscattering increases but not as much as when it is located at the top.

Figure 11 shows the dependence of backscatter on the relative shift (δ) calculated at a slightly smaller refractive index, $m_i = 1.25$, for the same values of

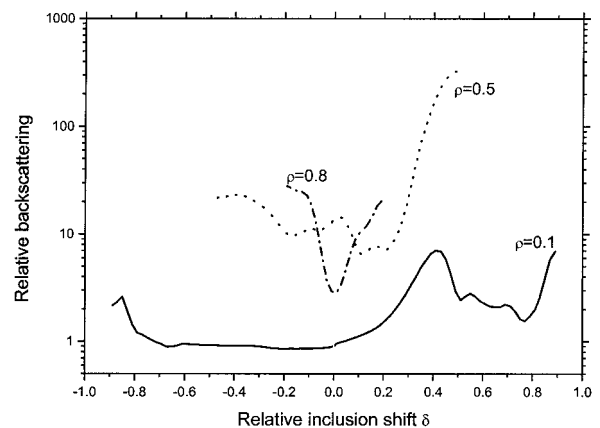


Fig. 10. Dependence of particle relative backscattering on the inclusion shift for inclusion relative radii of 0.1 (solid curve), 0.5 (dotted curve), and 0.8 (dashed-dotted curve). Computations are performed for log-normal distribution of host spheres' radii with $x_{\text{mean}} = 200$ and $\ln \sigma = 0.1$. Refractive indices of the host particle and inclusion are $m_h = 1.348$ and $m_i = 1.45$. The calculation step is $\Delta\delta = 0.02$, and the obtained results are smoothed over a 0.06 averaging interval.

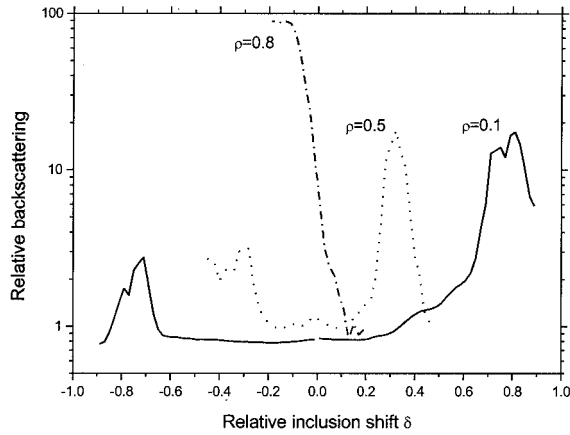


Fig. 11. Dependence of particle backscattering on the inclusion shift for inclusion relative radii of 0.1 (solid curve), 0.5 (dotted curve), and 0.8 (dashed-dotted curve). Computations are performed for log-normal distribution of host spheres' radii with $x_{\text{mean}} = 200$ and $\ln \sigma = 0.1$. Refractive indices of the host particle and inclusion are $m_h = 1.348$ and $m_i = 1.25$, respectively. The calculation step is $\Delta\delta = 0.02$, and the obtained results are smoothed with a 0.06 averaging interval.

inclusion relative radii as in Fig. 10. In contrast to Fig. 10, the behavior of the curves changes; the maximum relative backscattering is observed for an inclusion with $\rho \approx 0.8$ located near the bottom of the particle.

4. Application to a Case of a Water Droplet Containing an Ice Nuclear

As mentioned above, a case of special interest is a water sphere containing an ice inclusion. Two physical arrangements we have considered above are (i) the relative size of the ice and water mass and (ii) the location of the ice inclusion within the water drop. Here we first deal with the dependence of relative backscattering on the relative radius of the inclusion for an ice-water-mixed drop (Fig. 12). The figure shows the backscatter when the ice core is fixed to the top (solid curve) or to the bottom (dashed curve) of the host water sphere and the relative backscatter obtained for concentric spheres (dashed-dotted curve). Computations are performed for a log-normal distribution of the host spheres' radii with $x_{\text{mean}} = 400$, $\ln \sigma = 0.1$, and $m_i = 1.324$. Note that the refractive index of ice is lower than that of water, and, just as with the results of the previous section, the maximum backscattering is observed for an inclusion of $\rho \approx 0.85$ located near the bottom of a water sphere. Approximately a 50-fold enhancement in backscattering observed is limited to a narrow region of relative radius. For the inclusion located near the top of the host, the backscattering is characterized by an oscillating trend with smaller enhancements.

As we have already mentioned, the lidar ratio equals $R \approx 1/\beta$. For big ice inclusions ($\rho \approx 0.8$), this ratio is strongly decreased for the inclusion located near the bottom and increased for inclusions near the top of the water sphere. The translation of the in-

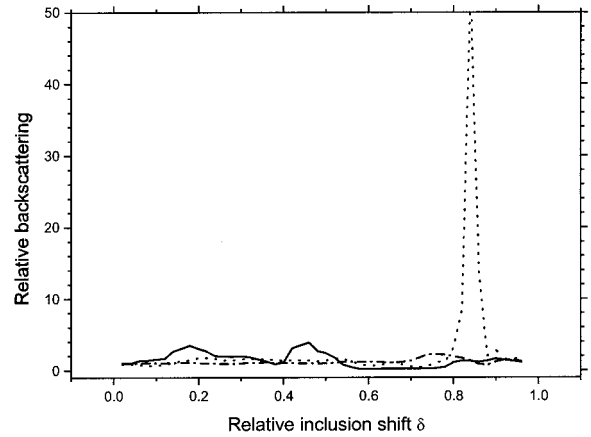


Fig. 12. Dependence of relative backscattering on the inclusion relative radius for an ice-water-combined particle. An ice sphere is fixed to the top (solid curve) or to the bottom (dotted curve) of the host water sphere, and a dashed-dotted curve shows the result obtained for concentric spheres. Computations are performed for log-normal distribution of host spheres' radii with $x_{\text{mean}} = 400$ and $\ln \sigma = 0.1$. The calculation step is $\Delta\rho = 0.02$, and the results for lidar ratio are smoothed with a 0.06 averaging interval.

clusion from the bottom to the top changes strongly the particle scattering properties, so the measurements of the lidar ratio of such a combined particle can, in principle, provide information about its structure.

In Fig. 13 we show the dependence of the relative backscatter enhancement as a result of the relative displacement of the ice inclusion from the center of the host particle for three distinct relative radius values ($\rho = 0.1$, $\rho = 0.5$, and $\rho = 0.85$). A general statement that can be made is that the smaller the inclusion, the smaller the enhancement, and it occurs at large displacements from the center. On the other hand, a large ice inclusion has little room for

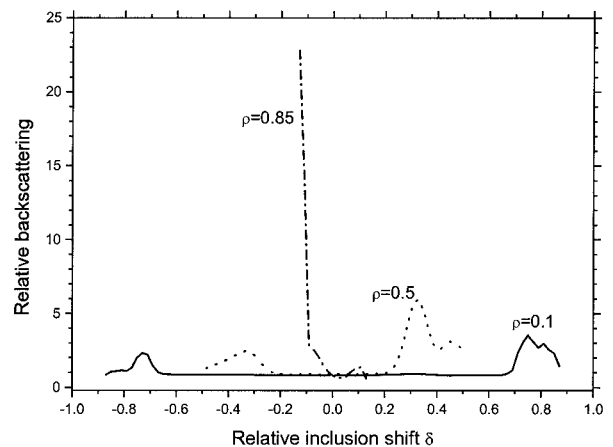


Fig. 13. Dependence of particle relative backscattering on the ice sphere relative shift for $\rho = 0.1$ (solid curve), 0.5 (dotted curve), and 0.85 (dashed-dotted curve). Computations are performed for log-normal distribution of host spheres' radii with $x_{\text{mean}} = 400$ and $\ln \sigma = 0.1$. Refractive indices of the host particle and inclusion are $m_h = 1.348$ and $m_i = 1.324$. The calculation step is $\Delta\delta = 0.02$.

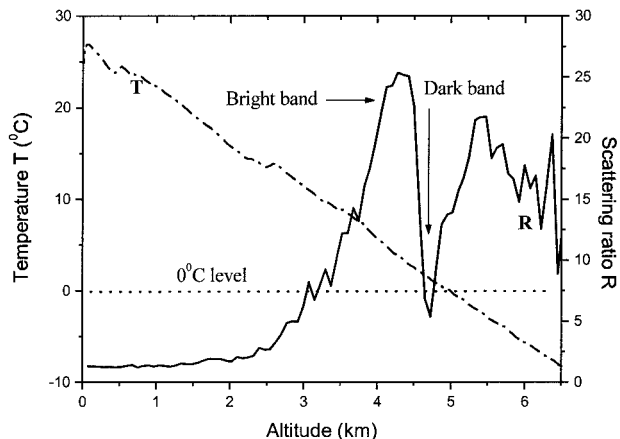


Fig. 14. Vertical profiles of temperature and scattering ratio illustrating lidar bright- and dark-band phenomena.

displacement from the center but has the largest backscatter enhancement.

In nature, an ice–water mixture occurs during the melting of a hail particle or snowflake as it falls and passes through increasingly warmer temperature layers. This is commonly recognized in radars as a narrow bright-band region.¹⁸ One factor for the bright-band observations in radars is the fact that enough water has melted to coat the ice in sufficient depth, as the low-density snowflakes melt and collapse to form drops and scatter as equivalent-sized water drops. Figure 14 shows the vertical profile of the scattering ratio (the ratio of the full backscattering to the molecular one) obtained from Raman lidar sounding of a snow cloud. The temperature profile was simultaneously measured with the sonde. The data were collected by the NASA scanning Raman lidar during the Third Convection and Moisture Experiment in 1998 at Andros Island, the Bahamas, during the passage of hurricane Bonnie.¹⁹ The experiment site was under a stratiform rain event that lasted several hours when the data were recorded. The strong scattering by large snow aggregates immediately above the melting layer ($z > 5$ km) results in a relative signal enhancement, and it goes down for $z > 5.5$ km because of strong attenuation by snowflakes.

However, the interesting phenomenon occurs just below this signal maximum, where the snow starts to melt and gets coated with water. A backscatter intensity minimum occurs in this melting layer region, where the hydrometeors are ice–water mixtures. It is on this region, in which snowflakes have sufficiently melted to form water-coated particles, that we focus. As the snowflakes melt, they collapse in size, resulting in a decrease in the backscattered lidar signal, reaching a minimum, before starting to increase. This increase may occur in the region in which wet snowflakes have collapsed into mixed-phase raindrops.

At the initial stage of the melting the nuclear may be located near the bottom because of air flow. The computations performed above show that backscattering

at such a geometry may be enhanced. When the nuclear becomes rather small, it may float to the top, and backscattering is decreased. So the decreasing of nuclear size and its shift from the bottom to the top may result in the feature similar to the bright band shown in Fig. 14 at altitude interval 3.5–4.5 km. It may be true that the ice–water mixture in a falling drop may not have the simple geometrical symmetry we have assumed but rather follows a complex mixture. Nevertheless, understanding the scattering patterns even in these simple geometrical formulations is important and can lead to further insights about the interaction of laser light with water–ice mixtures.

5. Conclusion

The extensive computer simulations were performed to understand the combined particles' backscattering properties as a function of inclusion location for different values of refractive index in the frame of the eccentric spheres model. The obtained results may be summarized as the following: Spherical inclusions with $m_i < m_h$ strongly increase backscattering when located near the host particle bottom; the relative inclusion radius corresponding to the maximal β is $\rho \sim 0.8$. For $m_i > m_h$ the backscattering enhancement is observed for the top inclusion location at $\rho \sim 0.5$. This β enhancement is specifically related to the eccentric inclusion location, whereas in the concentric geometry the backscattering increase is much smaller. The particle extinction does not depend significantly on inclusion position, so the rise of backscattering should be accompanied by a decrease of the lidar ratio. It is interesting that the lidar ratios should be different when measuring is done from aircraft and from the ground.

Though the study of microphysical processes in clouds with lasers implies calculations performed with size parameters in excess of 1000, to keep computation time manageable, we used in most cases $x_{\text{mean}} = 300$. But in some specific cases we performed the computations also with $x_{\text{mean}} = 500$ to make sure that the main observed features are preserved and do not depend significantly on particle size. Thus we are convinced that simulations are representative of real atmosphere phenomena and can be used to get an insight into the microphysical processes involving aerosol and clouds.

The developed computer code was applied to the simulation of scattering properties of melting ice spheres; we thus tried to get some understanding of lidar bright- and dark-band phenomena. The results demonstrate that the shift of the ice nuclear along the Z axis leads to the strong variations in the light backscattering coefficient and, in principle, may be responsible for the experimentally observed scattering enhancement. The analyzed model is rather idealized to describe the real situation. We do not consider the deformation of the water droplet and possible movement of the inclusion around inside the drop due to drag-induced internal circulations. The ice nuclear is suggested to be spherical, though in reality it is of complicated shape. Nevertheless, we can see a kind

of resemblance between the results of experimental measurements and our simulations. It may demonstrate the importance of eccentric nuclear position in the mechanism of lidar bright- and dark-band formation.

Appendix A

The extinction cross section is¹¹

$$\sigma_{\text{ext}} = -\frac{1}{2k^2 E_0^2} \text{Re} \left[\sum_{n=1}^{\infty} \sum_{m=-n}^n \frac{n(n+1)}{K_{nm}^2} (a_{nm} c_{nm}^* + a_{nm}^* c_{nm} + b_{nm}^* d_{nm} + b_{nm} d_{nm}^*) \right], \quad (\text{A1})$$

where

$$K_{nm} = \left[\frac{2n+1}{4\pi} \frac{(n-m)!}{(n+m)!} \right]^{1/2}.$$

Partial expression at fixed m is equal to

$$\sigma_{\text{ext},m} = -\frac{1}{2k^2 E_0^2} \text{Re} \left[\sum_{n=1}^{\infty} \frac{n(n+1)}{K_{nm}^2} (a_{nm} c_{nm}^* + a_{nm}^* c_{nm} + b_{nm}^* d_{nm} + b_{nm} d_{nm}^*) \right]. \quad (\text{A2})$$

This can be written in matrix form:

$$\sigma_{\text{ext},m} = -\frac{1}{2k^2 E_0^2} \text{Re}(\mathbf{B}^T \mathbf{N} \mathbf{C}^* + \mathbf{B}^{T*} \mathbf{N} \mathbf{C}), \quad (\text{A3})$$

where \mathbf{N} is a diagonal matrix of size $2N_{\text{max}} \times 2N_{\text{max}}$ with elements $[n(n+1)]/K_{nm}^2$, $n = 1, \dots, N_{\text{max}}$, $\mathbf{B}^T = \{a_{1,m}, \dots, a_{N_{\text{max}},m}, b_{1,m}, \dots, b_{N_{\text{max}},m}\}$ is a transpose of a column vector \mathbf{B} ; $\mathbf{C} = \{c_{1,m}, \dots, c_{N_{\text{max}},m}, d_{1,m}, \dots, d_{N_{\text{max}},m}\}$ is a row vector; and the wave number is $k = 2\pi/\lambda$.

In a similar way, a set of simultaneous equations¹¹ in matrix form is

$$\begin{aligned} \psi \mathbf{B} + \xi \mathbf{C} &= \mathbf{A} \mathbf{T}, \\ \psi' \mathbf{B} + \xi' \mathbf{C} &= \mathbf{A}' \mathbf{T}, \end{aligned} \quad (\text{A4})$$

where $\mathbf{B} = a_{1,m}, \dots, a_{N_{\text{max}},m}, b_{1,m}, \dots, b_{N_{\text{max}},m}$, $\mathbf{C} = c_{1,m}, \dots, c_{N_{\text{max}},m}, d_{1,m}, \dots, d_{N_{\text{max}},m}$, $\mathbf{T} = t_{1,m}, \dots, t_{N_{\text{max}},m}, u_{1,m}, \dots, u_{N_{\text{max}},m}$ are column vectors, ψ, ψ', ξ, ξ' are diagonal matrices of size $2N_{\text{max}} \times 2N_{\text{max}}$ consisting of Riccati–Bessel functions similar to matrix \mathbf{N} , and \mathbf{A} and \mathbf{A}' are square matrices containing constant coefficients at unknowns $t_{n,m}, u_{n,m}$.

Eliminating \mathbf{T} , we have equation $\mathbf{C} = \mathbf{M} \mathbf{B}$, where $\mathbf{M} = (\mathbf{A}^{-1} \xi - \mathbf{A}'^{-1} \xi')^{-1} (\mathbf{A}'^{-1} \psi' - \mathbf{A}^{-1} \psi)$, with \mathbf{A}^{-1} and \mathbf{A}'^{-1} as inverted matrices. Matrix \mathbf{M} does not depend on angle θ at which the incident wave impinges on the system j , but, for opposite angles θ_1 and $\theta_2 = 180^\circ - \theta_1$, the corresponding column vectors \mathbf{B}_1 and \mathbf{B}_2 are related as

$$\mathbf{B}_2 = \mathbf{D} \mathbf{B}_1, \quad (\text{A5})$$

where the diagonal matrix \mathbf{D} contains $(-1)^{m+1}$ in the upper half and $(-1)^m$ in the lower half of its diagonal. Taking into account Eqs. (A3) and (A5), we conclude that for opposite angles $\sigma_{\text{ext},m,1} = \sigma_{\text{ext},m,2}$; therefore

$$\sigma_{\text{ext},1} = \sigma_{\text{ext},2}. \quad (\text{A6})$$

References

1. M. Kerker, *The Scattering of Light and Other Electromagnetic Radiation* (Academic, New York, 1969), Chaps. 3 and 4.
2. K. Sassen, "Contrail-cirrus and their potential for regional climate change," *Bull. Am. Meteorol. Soc.* **78**, 1885–1903 (1997).
3. P. Di Girolamo, B. B. Demoz, and D. N. Whiteman, "Model simulations of melting hydrometeors: a new lidar bright band from melting frozen drops," *Geophys. Res. Lett.* **30**, 1626, doi: 10.1029/2002GL016825 (2003).
4. K. Sassen and T. Chen, "The lidar dark band: an oddity of the radar bright band," *Geophys. Res. Lett.* **22**, 3505–3508 (1995).
5. Q. L. Aden and M. Kerker, "Scattering of electromagnetic waves from two concentric spheres," *J. Appl. Phys.* **22**, 1242–1246 (1951).
6. T. Yokoyama and H. Tanaka, "Microphysical processes of melting snow-flakes detected by two-wavelength radar. Part I. Principle of measurement based on model calculation," *J. Meteorol. Soc. Jpn.* **62**, 650–666 (1984).
7. K. Aydin and Y. Zhao, "A computational study of polarimetric radar observables in hail," *IEEE Trans. Geosci. Remote Sens.* **28**, 412–422 (1990).
8. S. K. Mitra, O. Vohl, M. Ahr, and H. R. Pruppacher, "A wind tunnel and theoretical study of the melting behavior of atmospheric ice particles. IV: Experiment and theory for snow flakes," *J. Atmos. Sci.* **47**, 584–591 (1990).
9. R. Meneghini and L. Liao, "Effective dielectric constants of mixed-phase hydrometeors," *J. Atmos. Ocean. Technol.* **17**, 628–640 (2000).
10. J. G. Fikioris and N. K. Uzunoglu, "Scattering from an eccentrically stratified dielectric sphere," *J. Opt. Soc. Am.* **69**, 1359–1366 (1979).
11. D. W. Mackowski, "Analysis of radiative scattering for multiple sphere configurations," *Proc. R. Soc. London Ser. A* **433**, 599–614 (1991).
12. F. Borghese, P. Denti, R. Saija, and O. I. Sindoni, "Optical properties of spheres containing a spherical eccentric inclusion," *J. Opt. Soc. Am. A* **9**, 1327–1335 (1992).
13. N. C. Skaropoulos, M. P. Ioannidou, and D. P. Chrissoulidis, "Indirect mode-matching solution to scattering from a dielectric sphere with an eccentric inclusion," *J. Opt. Soc. Am. A* **11**, 1859–1866 (1994).
14. K. A. Fuller, "Scattering and absorption cross sections of compounded spheres. III. Spheres containing arbitrarily located spherical inhomogeneities," *J. Opt. Soc. Am. A* **12**, 893–904 (1995).
15. D. Ngo, G. Videen, and P. Chýlek, "A FORTRAN code for the scattering of EM waves by a sphere with a nonconcentric spherical inclusion," *Comput. Phys. Commun.* **1077**, 94–112 (1996).
16. J. D. Jackson, *Classical Electrodynamics*, 2nd ed. (Wiley, New York, 1975).
17. W. M. Irvine and J. B. Pollack, "Infrared optical properties of water and ice spheres," *Icarus* **8**, 324–360 (1968).
18. L. J. Battan, *Radar Observations of the Atmosphere* (Univ. Chicago Press, Chicago, Ill., 1973).
19. D. N. Whiteman, K. D. Evans, B. Demoz, D. O'C. Starr, E. W. Eloranta, D. Tobin, W. Feltz, G. J. Jedlovec, S. I. Gutman, G. K. Schwemmer, M. Cadirola, S. H. Melfi, and F. J. Schmidlin, "Raman lidar measurements of water vapor and cirrus clouds during the passage of hurricane Bonnie," *J. Geophys. Res.* **106**, 5211–5225 (2001).